Non peer-reviewed preprint submitted to Proceedings of the National Academy of Sciences

Predictability of abrupt northern-hemisphere cooling events during the last glacial

Takahito Mitsui[1,2] and Niklas Boers[1,2,3]

[1]Earth System Modelling, School of Engineering & Design, Technical University of Munich
[2]Potsdam Institute for Climate Impact Research, Telegraphenberg A31, Potsdam, 14473
[3]Department of Mathematics and Global Systems Institute, University of Exeter

Correspondence: takahito321@gmail.com

Predictability of abrupt northern-hemisphere cooling events during the last glacial

Takahito Mitsui[1,2], Niklas Boers[1,2,3]

[1]*Earth System Modelling, School of Engineering & Design, Technical University of Munich, Germany*

[2]*Potsdam Institute for Climate Impact Research, Telegraphenberg A31, Potsdam, 14473, Germany*

[3]*Department of Mathematics and Global Systems Institute, University of Exeter, UK*

Given the likely bistability of the Atlantic Meridional Overturning Circulation (AMOC) and its recently inferred weakening, it is important to investigate the capability of identifying robust precursor signals for a possible future AMOC collapse. Dansgaard-Oeschger (DO) events, manifested most clearly as abrupt Northern-Atlantic temperature jumps during glacial conditions, likely reflect past switches between strong and weak AMOC modes. Previous studies find statistical precursor signals for the DO warming transitions associated with a strengthening AMOC. Statistical precursor signals for the abrupt DO cooling transitions, presumably associated with AMOC transitions from the strong to the weak mode, have not been identified although these would be practically much more relevant given the concern of a future AMOC collapse. Here we identify robust and statistically significant precursor signals for several DO cooling transitions from Greenland ice core records, using the concept of critical slowing down. The main source of predictability stems from so-called rebound event, humps in the temperature observed at the end of interstadial, some decades to

centuries prior to the transition. Based on conceptual models, we propose several dynamical mechanisms producing such rebound events.

Significance Statement. Given the likely bistability of the Atlantic Meridional Overturning Circulation (AMOC) and its recently inferred weakening, it is crucial to investigate the capability of identifying precursor signals for a collapse of this key Atlantic ocean circulation system. In this study we find statistical precursor signals for past abrupt norhtern Atlantic cooling events that are supposedly associted with AMOC transitions to its weak state. We provide a theory that bridges the gap between observing statistical precursor signals and the precursor signs empirically known in paleoclimate research. Our results increase our confidence about the predictability of arguably the most relevant climate tipping point and provide new insights regarding tipping points in the climate system.

Introduction

A tipping point is a threshold in a forcing or control parameter, at which a small additional perturbation causes a qualitative change in the state of the system under consideration[1]. Once a tipping point is passed, a system can transition abruptly to an alternative stable or oscillatory state[2]. The existence of climate tipping points and the possibility of abrupt transitions had been theoretically predicted since the early 1960s[2,3]. Paleoclimate evidence supports that abrupt climate changes due to crossing tipping points actually occurred in the past[2,4–6]. Recent observational and modelling evidence suggest the existence of climate tipping elements in the present Earth, which pose arguably one of the greatest risks in the context of anthropogenic global warming[1,2]. The Atlantic

Meridional Overturning Circulation (AMOC) is considered the most important global-scale tipping element[1,2,6]. Recent studies have inferred that the AMOC is currently at its weakest in at least a millennium[7,8]; projections of the AMOC strength in the next hundred years are model-dependent, but the declining AMOC trend is projected to continue in the coming century[9].

The theory of critical slowing down (CSD) provides a framework to anticipate bifurcation-induced transitions[2,10–16]. The framework is based on the fact that the stability of a stable state is gradually lost as the system approaches the bifurcation point. Theoretically, the variance of the fluctuations around the fixed point diverges and the autocorrelation with a sufficiently small lag increases toward 1 at the critical point of a codimension-one bifurcation (Methods)[2,11,16]. Numerical studies show that these statistical precursor signals (SPS) can anticipate simulated AMOC collapses[17,18]. Moreover, based on further refined CSD indicators, evidence of stability loss in the North Atlantic in the course of the last century have been inferred from sea-surface temperature and salinity data, which might indicate that the observed AMOC weakening is indeed associated with a loss of stability[14]. To put these signals into context we investigate here if similar SPS can be detected also for past instances of AMOC collapse.

Dansgaard-Oeschger (DO) events are millennial-scale abrupt climate transitions during glacial intervals[19]. They are most clearly imprinted in the δ^{18}O and calcium ion concentration [Ca^{2+}] records from the Greenland ice cores (Fig. 1)[20,21]. The δ^{18}O and [Ca^{2+}] are interpreted as proxies for site temperature and atmospheric circulation changes, respectively. DO warmings occur typically within a few decades and are followed by gradual cooling during relatively warm glacial states termed interstadials, before a rapid return back to cold states referred to as stadials. The amplitude of the abrupt warming transitions ranges from 5 to 16.5°C (cf. ref. [22] and references therein). While the detailed mechanism of DO events remains debated[23–27], recent studies with general circulation models suggest that DO oscillations can spontaneously arise from complex interactions between the AMOC, ocean stratification, atmosphere and sea ice[28–33].

The DO events are considered the archetype of climate tipping behavior[2,4,6]. Early works found an SPS based on autocorrelation for one specific DO warming, the onset of Bølling–Allerød interstadial[5]. In following works, the existence of SPS for DO warmings was questioned considering that DO warmings are noise-induced rather than bifurcation-induced[34,35]. However a couple of later studies[13,36,37] detected SPS for several DO warmings either by ensemble averaging of CSD indicators for many events[36] or by using Wavelet-transform techniques focusing on a specific frequency band [13,37]. On the other hand, it has so far not been shown whether DO coolings are preceeded by characteristic CSD-based precursor signals as well. Given the recent AMOC weakening[7,8] and the observation-based suggestion that this weakening may be related to stability loss[14], it is important to investigate if CSD-based precursor signals can be detected for the DO cooling transitions as well, likely associated with past AMOC collapses. In view of the concern of a future AMOC collapse, such SPS of the DO coolings would in fact be practically more relevant than the already discovered SPS for the DO warmings.

In this study we explore CSD-based precursor signals for DO cooling transitions recorded in δ^{18}O and $\log_{10}[Ca^{2+}]$[20,21] from three Greenland Ice Cores: NGRIP, GRIP and GISP2 (see Fig. 1 for

NGRIP). Multiple records are used for a robust assessment because each has regional fluctuations as well as proxy- and ice-core-dependent uncertainties. The six records have been synchronized and are given at 20-yr resolution[20,21]. They continuously span the last 104 kyr b2k (kiloyears before 2000 CE), beyond which only NGRIP δ^{18}O is available up to a part of Eemian interglacial. In addition, we use a version of the NGRIP δ^{18}O and dust records at 5-cm depth resolution[38–40] in order to check the dependence of results on temporal resolutions, with the caveat that these high-resolution records span only the last 60 kyr.

We follow the classification of interstadials and stadials and associated timings of DO warming and cooling transitions by Rasmussen et al. (2014) [20], where Greenland interstadials (stadials) are labelled with 'GI' ('GS') with few exceptions below. A *rebound event* is a relatively abrupt warming often observed before an interstadial abruptly ends[41] (arrows in Figs. 1, 2 and 3). Generally a long rebound event accompanies a long interstadial ($R^2 = 0.95$,[41]). in Ref.[20,41], GI-14 and subsequent GI-13 are seen as one long interstadial with GI-13 consdered to be a strongly expressed rebound event ending GI-14 because the changes in δ^{18}O and $\log_{10}$[Ca^{2+}] during the quasi-stadail GS-14 do not reach the base-line levels of adjacent stadials. Similarly GI-23.1 and GI-22 are also seen as one long interstadial, and GI-22 is regarded as a rebound event (and GS-23.1 as quasi-stadial)[20,41]. Here we consider nine rebound-type events (Methods) including seven previously identified rebound events[20,41]. The start and end of each interstadial are identified at 20-yr resolution based on both δ^{18}O and [Ca^{2+}] in Ref.[20], where the uncertainties associated with the event timings are also estimated.

Results

Characteristic precursor signals of DO coolings. As CSD-based indicators we consider the variance and lag-1 autocorrelation, calculated in rolling windows across each interstadial (see Methods). Since this requires a minimum length of data points, we focus on interstadials longer than 1000 yr after removing 2σ uncertainty ranges of the transition timings (Fig. 1, gray shades). The removal of the 2σ uncertainty ranges of event timings (40 to 400 years) effectively excludes parts of the transitions themselves from the calculation of the CSD indicators. The resulting 12 interstadials ($>$1000 yr) of the NGRIP δ^{18}O record are magnified in Figs. 2 and 3 (top rows, blue). See SI Appendix, Figs. S1–S10 for the other records.

For each interstadial, the nonlinear trend is estimated with a local regression method, specifically the locally weighted scatterplot smoothing[42,43] (Figs. 2 and 3, top row, red). In this case the smoothing span α that defines the fraction of data points involved in the local regression is set to 50% of each segment length. Gaussian kernel smoothing gives similar results. The difference between the record and the nonlinear trend gives the approximately stationary residual fluctuations (second row). The CSD indicators are calculated from the residual series over a rolling window. In Figs. 2 and 3 the rolling window size W is set to 50% of each segment length (a default value in Ref.[5]). The smoothing span α and the rolling window size W are taken as fractions of individual interstadial length because time scales of local fluctuations (such as the duration of rebound events) change with the entire duration of interstadial. We examine the dependence of the results on α and W as part of our robustness tests.

The variance is plotted in the third row of Figs. 2 and 3. Positive trends in the variance are observed for 9 out of 12 interstadials; the individual trends are statistically significant in 6 out of 12 cases ($p < 0.05$), based on a null model assuming the same overall variance and autocorrelation, constructed by producing surrogates with randomized Fourier phases (See Methods). The lag-1 autocorrelation is also plotted for the same data in the bottom row. Positive trends in lag-1 autocorrelation are observed for 10 out of 12 interstadials, but are statistically significant only in 2 cases ($p < 0.05$). In several cases (GI-24.2, 21.1, 16.1, 14-13 and 12), the lag-1 autocorrelation first decreases and then increases. The drastic increases in both indicators near the end of the interstadials reflect the rebound events (arrows in Figs. 2 and 3). We obtain similar results for the other ice core records (SI Appendix, Figs. S1–S10). While we observe a number of positive trends for all the records, the number of detected statistically significant trends depends on the record and CSD indicator (SI Appendix, Table S1).

We check robustness of our results against changing smoothing span α and rolling window size W[43]. We calculate the p-value for the trend of each indicator changing the smoothing span between 20–70% of interstadial length (in steps of 10%) and the rolling window size between 20–60% (also in 10% steps), respectively. This yields a 6×5 matrix for the p-values: Example results, for GI-25 and δ^{18}O, are shown in Figs. 4a (variance) and 4b (lag-1 autocorrelation). The cross mark (x) indicates significant positive trends ($p < 0.05$) and the small open circle (o) indicates positive trend that are significant at 10% confidence but not at 5% confidence. Full results for the 12 interstadials, 6 records, and two CSD indicators are shown in SI Appendix, Figs. S11–S22. We consider positive trends in CSD indicators, i.e. the SPS of the transition, to be overall robust if we obtain significant positive trends ($p < 0.05$) for at least half (≥ 15) of the 30 parameter sets.

The robustness analysis is performed for all the long interstadials of the 6 records and the two CSD indicators (Fig. 4d). Among the 12 interstadials, we find at least one robust SPS for 9 interstadials (GI-25, 23.1, 21.1, 20, 19.2, 16, 14, 12 and 8) and multiple robust SPS for 6 (GI-25, 23.1, 21.1, 14, 12 and 8). If the data series is a stationary stochastic process, the probability of observing a robust SPS is estimated to be 5% (Methods). Thus the observation of robust SPS for 36 cases (31%) over the 116 combinations of data and indicators in Fig. 4d is very unlikely to occur by chance. Robust SPS are more likely to be observed in longer interstadials than in shorter ones (compare Figs. 4c and 4d).

Further sensitivity analyses. We examine how much the rebound events affect the detection of CSD-based SPS. For this purpose CSD indicators are again calculated excluding the rebound events and their preceding cold spells (Methods). Only four interstadials (GI-23.1, 14, 12 and 8) exhibit robust SPS without the rebound events, while 8 interstadials (GI-25, 23.1, 21.1, 20, 16, 14, 12 and 8) exhibit robust SPS with the rebound events included (SI Appendix, Fig. 23). The rebound events should hence be considered important, sometimes indispensable, sources for SPS of DO coolings.

We also examine the dependence of the results on the time resolution of the data. Here we use a high-resolution (5-cm depth) δ^{18}O record[38,39] and a dust record[40] from the NGRIP over the last 60 kyr. Since the data in these records are non-uniform in time, they are linearly resampled every 5 yr before calculating CSD indicators. We focus on 11 interstadials longer than 300 yr in order to have enough data points. For the dust record, three interstadials (GI-15, 8 and 7) are excluded from the analysis because the original data has long parts of missing values. The CSD indicators, calculated with a smoothing span of $\alpha = 50\%$ and rolling windows with $W = 50\%$, are shown in SI Appendix, Figs. S24–S27. Through the robustness analyses with respect to α and W, we find at least one robust SPS for 3 out of 11 interstadials (SI Appendix, Fig. S28). The robust SPS for GI-14-13 and GI-12 from the high-resolution records are consistent with those from the 20-yr resolution records. Moreover for GI-1, the high-resolution δ^{18}O record exhibits a robust SPS in terms of lag-1 autocorrelation, although the 20-yr resolution record does not. Again, shorter interstadials ($\lesssim$1000 yr) do not show robust SPS.

Discussion

We detected robust precursor signals of DO cooling transitions for more than half of the long ($>$1000 yr) interstadials, but not for shorter interstadials. The results suggest that long interstadials, the existence of rebound events, and the presence of precursor signals for the DO cooling transitions at the end of interstadials are related (except for GI-19.2, which has no noticeable rebound event). These aspects may be related to generic properties of nonlinear dynamical systems. On the basis of conceptual mathematical models (Methods), we propose four possible dynamical mechanisms leading to the precursor signals of DO cooling transitions. In three out of four mechanisms, oscillations like the rebound events can systematically arise prior to the abrupt cooling transitions. These modelling results justify the inclusion of the rebound events in the search for precursor signals presented above.

1. The fold bifurcation mechanism. Since the pioneering work by Stommel[3], the AMOC is considered to exhibit bistability[4,44]. The bistability of the AMOC strength x may be conceptually modelled by a double-fold bifurcation model: $\dot{x} = f(x)+p+\xi(t)$, where $f(x)$ has two fold points like $x - x^3$ and $|x|(1-x)$. Here we take the quadratic from $f(x) = |x|(1-x)$, but the following arguments are qualitatively the same for $x - x^3$. The parameter p represents the surface salinity flux (i.e. negative freshwater flux), and $\xi(t)$ denotes white Gaussian noise. The unperturbed model for $\xi(t) = 0$ has equilibria on an S-shaped curve: $f(x) + p = 0$ (Fig. 5a, green). The state $x(t)$ initially on the upper stable branch jumps down to the lower stable branch as p decreases across the fold bifurcation point at $p = -0.25$. The variance and the autocorrelation of the local fluctuations (i.e. the CSD indicators) increase as p approaches the fold bifurcation point[2,11].

2. Stochastic slow-fast oscillation mechanism. The FitzHugh-Nagumo (FHN) system is a prototypical model for slow-fast oscillations and excitability[45]. It is often invoked for conceptual models of DO oscillations[29,46–49]. An FHN-type model of DO oscillations is obtained by introducing a slow variable y into the fold bifurcation model: $\dot{x} = \frac{1}{\tau_x}(|x|(1-x) + y + p) + \xi(t)$, $\dot{y} = \frac{1}{\tau_y}(-x - y)$, where τ_x and τ_y are time-scale parameters ($\tau_x \ll \tau_y$). Invoking the salt-oscillator hypothesis for DO oscillations suggested by the comprehensive climate model simulations that are successful in reproducing DO cycles[50], we may interpret y as the salinity in the polar halocline surface mixed layer, which gradually decreases (increases) when the AMOC intensity x is strong (weak). Here we consider the case that the unperturbed system is excitable. For example for $p = 0.26$, the unperturbed system has a stable equilibrium near the upper fold point of the S-shaped critical manifold, $\{(x, y) \in \mathbb{R}^2 \,|\, y = -|x|(1-x) - p\}$ (Fig. 5c, green), but stochastic oscillations

sustain under the dynamical noise forcing $\xi(t)$ (Figs. 5b and 5c, blue). Due to the time-scale separation ($\tau_x \ll \tau_y$), the oscillations occur along the attracting parts of the critical manifold (Fig. 5c). Because y is much slower than x, the dynamics of x is similar to the dynamics of the fold bifurcation model with slowly changing y. Consequently SPS can be observed near the fold point of the critical manifold (SI Appendix, Fig. S29). The increase of the variance prior to the transitions in the FHN model is reported also in Ref.[51]. Since the unperturbed system has an equilibrium near the upper fold point, the motion is stagnant near the fold point. This provides favorable conditions for observing SPS. The state jumps from the upper branch of the critical manifold to its lower blanch often after an upward jump induced by noise. These upward jumps resemble the rebound events prior to DO coolings. The overall phenomenon is the same in the self-sustained oscillation regime of the FHN model as long as the equilibrium locates near the fold point of the critical manifold.

3. Hopf bifurcation mechanism. In contrast to the fold bifurcation, the Hopf bifurcation manifests oscillatory instability[52]. In several ocean box models, the thermohaline circulation is destabilized via a Hopf bifurcation rather than a fold bifurcation[53–55]. It is also considered a potential generating mechanism of DO oscillations in a low-order coupled climate model[56] and in a comprehensive climate model[28]. Assume that the parameter p decreases slowly in the FHN-type model (Figs. 5d and 5e). The underlying dynamics changes from the stable equilibrium to the limit-cycle oscillations at the Hopf bifurcation point $p = (1 - \tau_x/\tau_y)^2/4$ (Methods). If stochastic forcing is added to the system, noise-induced small oscillations can appear prior to the onset of the limit-cycle oscillations (Fig. 5d and 5e). The precursor oscillations resemble rebound events, while their shape depends on the noise. Again SPS can be observed near the Hopf bifurcation point (SI

Appendix, Fig. S30)[2,16,51].

4. Mixed-mode oscillation mechanism. Mixed-mode oscillations (MMOs) are periodic oscillations consisting of small and large-amplitude oscillations[57]. They often arise in systems with one fast variable and two slow variables[57]. For example, MMOs appear in the FHN-type model with a slight extension: $\dot{x} = \frac{1}{\tau_x}(|x|(1-x)+y+p)$, $\dot{y} = \frac{1}{\tau_y}(-x-y+k(z-y))$ and $\dot{z} = \frac{1}{\tau_z}(-x-z+k(y-z))$, where z is another slow variable with time scale τ_z ($\gg \tau_x$) and k is the diffusive-coupling constant between slow variables. We interpret y as the surface salinity in the North Atlantic convection region that directly affects the AMOC strength x again, and z as the surface salinity outside the convection region that affects the surface salinity y in the convection region via mixing. For specific parameter settings (Methods), the system has an unstable equilibrium $(x, y, z) = (\sqrt{p}, -\sqrt{p}, -\sqrt{p})$ of saddle-focus type, with one stable direction with a negative real eigenvalue and a two-dimensional unstable manifold with complex eigenvalues with positive real part. The slow-fast oscillations occur along the critical manifold $\{(x, y, z) \in \mathbb{R}^3 \,|\, y = -|x|(1-x)-p\}$ (Figs. 5f and 5g). However, due to the saddle-focus equilibrium on the critical manifold, the trajectory is attracted toward the saddle from the direction of the stable manifold (black segment) and repelled from it in a spiralling fashion. The striking point is the systematic occurrence of small-amplitude oscillations prior to the abrupt transition, which also resemble the rebound events prior to the DO cooling transitions. A more realistic time series is obtained if an observation noise is added on $x(t)$ (SI Appendix, Fig. S31). Then SPS can be stably observed near the fold point of the critical manifold.

We have proposed four possible dynamical mechanisms for the DO cooling transitions that can manifest precursor signals and behavior resembling the rebound events found in the ice core records: The precursor signals for the DO coolings can be (i) strict critical slowing down due to the approaching of a fold bifurcation, (ii) critical slowing down in a wider sense, in stochastic slow-fast oscillations, (iii) noise-induced oscillations prior to Hopf bifurcations, or (iv) the signal of mixed-mode oscillations. While the details of these mechanisms are different, they are all related to the fold points of the equilibrium curve or the critical manifolds. Consequently the precursor signals can be detected by the conventional CSD indicators. Note that the precursor behavior like the rebound events occur when the modelled interstadials have equilibria on the critical manifold with marginal stability (i.e., the equilibrium has neither strong stability leading to a permanent state nor strong instability leading to brief interstadials) (Figs. 5b–5g). Then the duration of the modelled interstadial is comparatively long in relation to the marginal stability. This provides an explanation why the rebound events in the ice core records and significant precursor signals are observed only for long interstadials ($\gtrsim 1000$ yr).

In summary, we have provided robust evidence that the DO cooling transitions from interstadial to stadial glacial conditions are preceded by characteristic precursor signals due to CSD. These signals are robust across CSD indicators, ice core records and proxy variables. Rebound events prior to the cooling transitions are important in producing the statistical precursor signals. We have proposed four different dynamical mechanisms to explain the role of these rebound events and more generally to understand the physical reasons for the revealed predictability of the DO cooling transitions. Because these transitions are most likely associated with AMOC collapses, our results provide empirical evidence from past climate records that it should indeed be possible to anticipate AMOC transitions from the strong to the weak mode based on CSD indicators.

Methods

Data: Greenland ice core records. We use δ^{18}O and $\log_{10}[Ca^{2+}]$ records[20,21] from Greenland ice cores: NGRIP, GRIP and GISP2. These records have been synchronized and are published at 20-yr resolution. They continuously span the last 104 kyr b2k, beyond which only NGRIP δ^{18}O is available up to a part of Eemian interglacial. In addition to the 20-yr-resolution records, we also use high-resolution (5-cm depth) δ^{18}O[38,39] and dust [40] records from the NGRIP over the last 60 kyr. We use the classification of Greenland interstadials (GI) and stadials (GS) by Rasmussen et al. (2014)[20].

A *rebound event* is an abrupt warming often observed before an interstadial abruptly ends[41]. Capron et al. (2010) describe warmings at the end of interstadials GI-11, GI-12, GI-16 and GI-21 as rebound events and also GI-13 and GI-22 as rebound events[41]. Consequently, the composition of GI-14, GS-14 and GI-13 is considered one long interstadial, and also the composition of GI-23.1, GS-23.1 and GI-22 is considered one long interstadial[20,41]. GI-20a is also recognized as a rebound event in Ref.[20]. Given that the rebound events are warmings following a colder spell during interstadial conditions that does not reach the stadial levels[20], we regard the following nine epochs as rebound-type events: GI-8a, the hump at the end of GI-11 (42240–$\sim$42500 yr b2k), GI-12a, GI-13, the hump at the end of GI-16.1 (56500–$\sim$56900 yr b2k), GI-20a, GI-21.1c-b-a (two warming transitions), GI-22 and GI-25a. When we examine the effect of rebound events on our results, we exclude the entire parts including the cold spells prior to the rebound events.

The start (warming) and end (cooling) of each DO event are identified in 20-yr resolution based on both δ^{18}O and [Ca^{2+}] in Ref.[20]. The estimated uncertainty of event timing varies event by event. We remove the 2σ uncertainty range of the event timing (40 to 400 years) estimated in Ref.[20] from our calculation of CSD indicators.

Statistical indicators of critical slowing down. Based on the theory of critical slowing down (CSD), we posit that the stability of a dynamical system perturbed by noise is gradually lost as the system approaches a bifurcation point[2,11,16]. For the fold bifurcation, the variance of the fluctuations around a local stable state diverges and the autocorrelation function of the fluctuations increases toward 1 at any lag τ. The same is true for the transcritical as well as the pitchfork bifurcation[2,16]. For the Hopf bifurcation, the variance increases, but the autocorrelation function of the form $C(\tau) = e^{\mu|\tau|\cos\omega\tau}$ may increases or decreases depending on τ, where μ and $\pm\omega i$ are the real and imaginary parts of the complex eigenvalues of the Jacobian matrix of the local linearized system[2,16]. Nevertheless the autocorrelation function $C(\tau)$ increases for sufficiently small τ. These characteristics can be used to anticipate abrupt transitions cause by codimension-one bifurcations. For time discrete series, we follow previous studies and calculate lag-1 autocorrelation.

Prior to calculating CSD indicators, we estimate the local stable state by using a local regression method called the locally weighted scatterplot smoothing (LOESS)[42,43]. The polynomial degree is set to 1, i.e., the smoothing is performed with the local linear fit. The smoothing span parameter α that defines the fraction of data points involved in the local regression is set to 50% of each segment length in Figs. 2 and 3. However, we examine the dependence of results on α over the range 20–70%. The difference between the record and the smoothed one gives the residual fluctuations. The CSD indicators, i.e., variance and lag-1 autocorrelation, are calculated for the residuals over a rolling window. The size of this rolling window is set to 50% of the record in Figs. 2 and 3, but it is changed over the range 20–60% to test robustness.

Probability of observing robust precursor signals. The statistical significance of precursor signals of critical transitions, in terms of positive trends of CSD indicators, is assessed by hypothesis testing[13,37,43,58]. We consider as null model a stationary stochastic process with preserved variance and autocorrelation. The n surrogate data are prepared form the original residual data series by the phase-randomization method, thus preserving the variance and autocorrelation function of the original time series via Wiener-Khinchin theorem. Here we take $n = 1000$. The linear trend (a_0) of the CSD indicator for the original residual time series and the linear trends (a_s) of CSD indicators for the surrogate data are calculated. We consider the precursor signal of the original series statistically significant if the probability of $a_s > a_o$ (p-value) is less than 0.05. Thus, if the original data is already a stationary stochastic process (exhibiting no CSD), one should expect spuriously significant results at a probability of 0.05 by definition. In principle this is independent of the smoothing span α as well as the rolling window size W used for calculating CSD indicators. We consider a precursor signal robust if we find at least 15 significant cases ($p < 0.05$) for 30 combinations of α and W. Then the probability of observing a robust precursor signal can be shown to be 0.05. In order to check this numerically, we generate 5000 surrogates of the original

δ^{18}O series of interstadial GI-25 and calculate the probability of finding robust precursor signals. The resulting fractions are 0.044 for the variance and 0.042 for the lag-1 autocorrelation, which are close to 0.05. For the case of GI-12, we obtain 0.042 for the variance and 0.052 for the lag-1 autocorrelation, again close to 0.05. These results support that the probability of observing a robust precursor signal is 5% if the data are stationary stochastic processes.

Candidate mechanisms for DO cooling transitions. Here we describe specific settings for four conceptual models representing different candidate mechanisms for the DO cooling transitions. Stochastic differential equations below are solved with the Euler-Maruyama method with step size of 10^{-3}.

1. The bistability of the AMOC strength x can be conceptually modelled by a double-fold bifurcation model: $\dot{x} = f(x) + p + \xi(t)$, where $f(x)$ has two fold points. Here for f one can use either $f(x) = x - x^3$ or $f(x) = |x|(1 - x)$. We take the quadratic function $f(x) = |x|(1 - x)$ that arises in the original Stommel model[3,4,44]. The parameter p represents the surface salinity flux (i.e., negative freshwater flux). $\xi(t)$ is white Gaussian noise, e.g. freshwater perturbations or weather forcing. In Fig. 5a, the initial condition is taken at $x(0) = 1.1$, near the upper stable fixed point of the unperturbed system. The parameter p is then slowly decreased from 0.1 to -0.4 over the period from $t = 0$ to 500, to trigger the bifurcation-induced transition.

2. The FitzHugh-Nagumo-type (FHN-type) system is a prototypical model of slow-fast oscillators and often invoked for conceptual models of DO oscillations[29,46–49]. The FHN-type model subjected to dynamical noise is obtained by introducing a slow variable y into the fold bifurcation

model: $\dot{x} = \frac{1}{\tau_x}(|x|(1-x)+y+p)+\xi(t)$, $\dot{y} = \frac{1}{\tau_y}(-x-y)$, where τ_x and τ_y are time-scale parameters ($\tau_x \ll \tau_y$). Following the salt-oscillator hypothesis to explain DO cycles[50], we may interpret y as the salinity in the polar halocline surface mixed layer, which decreases (increases) when the AMOC is strong (weak). In turn, the decreased (increased) surface salinity y inhibits (promotes) convective activity and weakens (strengthens) the AMOC x. In the case of Figs. 5b and 5c we set $p = 0.26$, $\tau_x = 0.01$, $\tau_y = 1$ and $\langle \xi_x^2 \rangle = 0.3$. The x-nullcline (critical manifold) of the unperturbed system is $y = -|x|(1-x)-p$ (Fig. 5c, green) and the y-nullcline is the $y = -x$ (Fig. 5c, magenta dashed). The intersection of the x- and y-nullclines is the equilibrium point of the unperturbed system $(\sqrt{p}, -\sqrt{p})$, which is near the fold point of the critical manifold in this parameter setting.

3. For demonstrating the Hopf bifurcation mechanism in Figs. 5d and 5e, the same stochastic FHN-type model is used with $\tau_x = 0.01$, $\tau_y = 1$ and $\langle \xi^2 \rangle = 0.05$, but here p is gradually decreased from 0.3 to 0.2, over a period of 10 time units. For $0.2 < p < 0.3$, the underlying deterministic system has a unique equilibrium point at $(x, y) = (\sqrt{p}, -\sqrt{p})$. The Hopf bifurcation of the equilibrium occurs if the complex eigenvalues of the Jacobian matrix at the equilibrium passes the imaginary axis[52]. In the present case, the eigenvalues are $\lambda_\pm = \frac{1}{2}\left\{\frac{1-2\sqrt{p}}{\tau_x} - \frac{1}{\tau_y} \pm \sqrt{(\frac{1-2\sqrt{p}}{\tau_x} - \frac{1}{\tau_y})^2 - \frac{8\sqrt{p}}{\tau_x\tau_y}}\right\}$, which are complex for $\frac{1}{4}(1+\frac{\tau_x}{\tau_y} - 2\sqrt{\frac{\tau_x}{\tau_y}})^2 < p < \frac{1}{4}(1+\frac{\tau_x}{\tau_y} + 2\sqrt{\frac{\tau_x}{\tau_y}})^2$. In this range of p, the real part of $\lambda_\pm$ changes from negative to positive at the Hopf bifurcation point: $p_H = (1-\tau_x/\tau_y)^2/4$. For $\tau_x/\tau_y = 0.01$, $p_H = 0.245025$.

4. The mixed-mode oscillation model is obtained if the FHN-type model is extended to have multiple interacting slow variables. E.g., $\dot{x} = \frac{1}{\tau_x}(|x|(1-x)+y+p)$, $\dot{y} = \frac{1}{\tau_y}(-x-y+k(z-y))$

and $\dot{z} = \frac{1}{\tau_z}(-x - z + k(y - z))$, where z is another slow variable with time scale τ_z ($\gg \tau_x$) and k is the diffusive coupling constant between slow variables. We interpret y as the surface salinity in the North Atlantic convection region, which directly affects the AMOC strength x, and z as the surface salinity outside the convection region that affects the surface salinity y in the convection region via mixing. We set $\tau_x = 0.02$, $\tau_y = 2$, $\tau_z = 4$, $p = 0.225$ and $k = 0.8$. This system has an unstable equilibrium $(x, y, z) = (\sqrt{p}, -\sqrt{p}, -\sqrt{p})$ of saddle-focus type, with one stable direction with a negative real eigenvalue -0.67 and a two-dimensional unstable manifold with complex conjugate eigenvalues with positive real part $0.94 \pm 4.7i$.

Reference

1. Armstrong McKay, D. I. *et al.* Exceeding 1.5 c global warming could trigger multiple climate tipping points. *Science* **377**, eabn7950 (2022).

2. Boers, N., Ghil, M. & Stocker, T. F. Theoretical and paleoclimatic evidence for abrupt transitions in the earth system. *Environmental Research Letters* **17**, 093006 (2022).

3. Stommel, H. Thermohaline convection with two stable regimes of flow. *Tellus* **13**, 224–230 (1961).

4. Alley, R. B. *et al.* Abrupt climate change. *science* **299**, 2005–2010 (2003).

5. Dakos, V. *et al.* Slowing down as an early warning signal for abrupt climate change. *Proceedings of the National Academy of Sciences* **105**, 14308–14312 (2008).

6. Brovkin, V. *et al.* Past abrupt changes, tipping points and cascading impacts in the earth system. *Nature Geoscience* **14**, 550–558 (2021).

7. Rahmstorf, S. *et al.* Exceptional twentieth-century slowdown in atlantic ocean overturning circulation. *Nature climate change* **5**, 475–480 (2015).

8. Caesar, L., Rahmstorf, S., Robinson, A., Feulner, G. & Saba, V. Observed fingerprint of a weakening atlantic ocean overturning circulation. *Nature* **556**, 191–196 (2018).

9. Masson-Delmotte, V. *et al.* Climate change 2021: the physical science basis. *Contribution of working group I to the sixth assessment report of the intergovernmental panel on climate change* **2** (2021).

10. Carpenter, S. R. & Brock, W. A. Rising variance: a leading indicator of ecological transition. *Ecology letters* **9**, 311–318 (2006).

11. Scheffer, M. *et al.* Early-warning signals for critical transitions. *Nature* **461**, 53–59 (2009).

12. Kuehn, C. A mathematical framework for critical transitions: normal forms, variance and applications. *Journal of Nonlinear Science* **23**, 457–510 (2013).

13. Boers, N. Early-warning signals for dansgaard-oeschger events in a high-resolution ice core record. *Nature communications* **9**, 2556 (2018).

14. Boers, N. Observation-based early-warning signals for a collapse of the atlantic meridional overturning circulation. *Nature Climate Change* **11**, 680–688 (2021).

15. Boers, N. & Rypdal, M. Critical slowing down suggests that the western greenland ice sheet is close to a tipping point. *Proceedings of the National Academy of Sciences* **118**, e2024192118 (2021).

16. Bury, T. M., Bauch, C. T. & Anand, M. Detecting and distinguishing tipping points using spectral early warning signals. *Journal of the Royal Society Interface* **17**, 20200482 (2020).

17. Boulton, C. A., Allison, L. C. & Lenton, T. M. Early warning signals of atlantic meridional overturning circulation collapse in a fully coupled climate model. *Nature communications* **5**, 1–9 (2014).

18. Held, H. & Kleinen, T. Detection of climate system bifurcations by degenerate fingerprinting. *Geophysical Research Letters* **31** (2004).

19. Dansgaard, W. *et al.* Evidence for general instability of past climate from a 250-kyr ice-core record. *Nature* **364**, 218–220 (1993).

20. Rasmussen, S. O. *et al.* A stratigraphic framework for abrupt climatic changes during the last glacial period based on three synchronized greenland ice-core records: refining and extending the intimate event stratigraphy. *Quaternary Science Reviews* **106**, 14–28 (2014).

21. Seierstad, I. K. *et al.* Consistently dated records from the greenland grip, gisp2 and ngrip ice cores for the past 104 ka reveal regional millennial-scale δ 18 o gradients with possible heinrich event imprint. *Quaternary Science Reviews* **106**, 29–46 (2014).

22. Kindler, P. *et al.* Temperature reconstruction from 10 to 120 kyr b2k from the ngrip ice core. *Climate of the Past* **10**, 887–902 (2014).

23. Broecker, W. S., Peteet, D. M. & Rind, D. Does the ocean-atmosphere system have more than one stable mode of operation? *Nature* **315**, 21–26 (1985).

24. Ganopolski, A. & Rahmstorf, S. Rapid changes of glacial climate simulated in a coupled climate model. *Nature* **409**, 153–158 (2001).

25. Petersen, S. V., Schrag, D. P. & Clark, P. U. A new mechanism for dansgaard-oeschger cycles. *Paleoceanography* **28**, 24–30 (2013).

26. Dokken, T. M., Nisancioglu, K. H., Li, C., Battisti, D. S. & Kissel, C. Dansgaard-oeschger cycles: Interactions between ocean and sea ice intrinsic to the nordic seas. *Paleoceanography* **28**, 491–502 (2013).

27. Boers, N., Ghil, M. & Rousseau, D.-D. Ocean circulation, ice shelf, and sea ice interactions explain dansgaard–oeschger cycles. *Proceedings of the National Academy of Sciences* 201802573 (2018).

28. Peltier, W. R. & Vettoretti, G. Dansgaard-oeschger oscillations predicted in a comprehensive model of glacial climate: A "kicked" salt oscillator in the atlantic. *Geophysical Research Letters* **41**, 7306–7313 (2014).

29. Vettoretti, G., Ditlevsen, P., Jochum, M. & Rasmussen, S. O. Atmospheric co2 control of spontaneous millennial-scale ice age climate oscillations. *Nature Geoscience* **15**, 300–306 (2022).

30. Brown, N. & Galbraith, E. D. Hosed vs. unhosed: interruptions of the atlantic meridional overturning circulation in a global coupled model, with and without freshwater forcing. *Climate of the Past* **12** (2016).

31. Klockmann, M., Mikolajewicz, U., Kleppin, H. & Marotzke, J. Coupling of the subpolar gyre and the overturning circulation during abrupt glacial climate transitions. *Geophysical Research Letters* **47**, e2020GL090361 (2020).

32. Zhang, X. *et al.* Direct astronomical influence on abrupt climate variability. *Nature Geoscience* **14**, 819–826 (2021).

33. Kuniyoshi, Y., Abe-Ouchi, A., Sherriff-Tadano, S., Chan, W.-L. & Saito, F. Effect of climatic precession on dansgaard-oeschger-like oscillations. *Geophysical Research Letters* **49**, e2021GL095695 (2022).

34. Ditlevsen, P. D. & Johnsen, S. J. Tipping points: early warning and wishful thinking. *Geophysical Research Letters* **37** (2010).

35. Lenton, T., Livina, V., Dakos, V. & Scheffer, M. Climate bifurcation during the last deglaciation? *Climate of the Past* **8**, 1127–1139 (2012).

36. Cimatoribus, A., Drijfhout, S., Livina, V. & Van Der Schrier, G. Dansgaard–oeschger events: bifurcation points in the climate system. *Climate of the Past* **9**, 323–333 (2013).

37. Rypdal, M. Early-warning signals for the onsets of greenland interstadials and the younger dryas–preboreal transition. *Journal of Climate* **29**, 4047–4056 (2016).

38. members, N. G. I. C. P. *et al.* High resolution record of northern hemisphere climate extending into the last interglacial period. *Nature* **431**, 147–151 (2004).

39. Gkinis, V., Simonsen, S. B., Buchardt, S. L., White, J. & Vinther, B. M. Water isotope diffusion rates from the northgrip ice core for the last 16,000 years–glaciological and paleoclimatic implications. *Earth and Planetary Science Letters* **405**, 132–141 (2014).

40. Ruth, U., Wagenbach, D., Steffensen, J. P. & Bigler, M. Continuous record of microparticle concentration and size distribution in the central greenland ngrip ice core during the last glacial period. *Journal of Geophysical Research: Atmospheres* **108** (2003).

41. Capron, E. *et al.* Millennial and sub-millennial scale climatic variations recorded in polar ice cores over the last glacial period. *Climate of the Past* **6**, 345–365 (2010).

42. Cleveland, W., Grosse, E. & Shyu, W. Local regression models. chapter 8 in statistical models in s (jm chambers and tj hastie eds.), 608 p. *Wadsworth & Brooks/Cole, Pacific Grove, CA* (1992).

43. Dakos, V. *et al.* Methods for detecting early warnings of critical transitions in time series illustrated using simulated ecological data. *PloS one* **7**, e41010 (2012).

44. Rahmstorf, S. Ocean circulation and climate during the past 120,000 years. *Nature* **419**, 207–214 (2002).

45. FitzHugh, R. Impulses and physiological states in theoretical models of nerve membrane. *Biophysical journal* **1**, 445 (1961).

46. Roberts, A. & Saha, R. Relaxation oscillations in an idealized ocean circulation model. *Climate dynamics* **48**, 2123–2134 (2017).

47. Mitsui, T. & Crucifix, M. Influence of external forcings on abrupt millennial-scale climate changes: a statistical modelling study. *Climate Dynamics* **48**, 2729–2749 (2017).

48. Lohmann, J. & Ditlevsen, P. D. A consistent statistical model selection for abrupt glacial climate changes. *Climate dynamics* **52**, 6411–6426 (2019).

49. Riechers, K., Mitsui, T., Boers, N. & Ghil, M. Orbital insolation variations, intrinsic climate variability, and quaternary glaciations. *Climate of the Past* **18**, 863–893 (2022).

50. Vettoretti, G. & Peltier, W. R. Fast physics and slow physics in the nonlinear dansgaard–oeschger relaxation oscillation. *Journal of Climate* **31**, 3423–3449 (2018).

51. Meisel, C. & Kuehn, C. Scaling effects and spatio-temporal multilevel dynamics in epileptic seizures. *PLoS One* **7**, e30371 (2012).

52. Strogatz, S. H. *Nonlinear dynamics and chaos: with applications to physics, biology, chemistry, and engineering* (CRC Press, 2018).

53. Alkhayuon, H., Ashwin, P., Jackson, L. C., Quinn, C. & Wood, R. A. Basin bifurcations, oscillatory instability and rate-induced thresholds for atlantic meridional overturning circulation in a global oceanic box model. *Proceedings of the Royal Society A* **475**, 20190051 (2019).

54. Abshagen, J. & Timmermann, A. An organizing center for thermohaline excitability. *Journal of physical oceanography* **34**, 2756–2760 (2004).

55. Sakai, K. & Peltier, W. R. A dynamical systems model of the dansgaard-oeschger oscillation and the origin of the bond cycle. *Journal of climate* **12**, 2238–2255 (1999).

56. Timmermann, A., Gildor, H., Schulz, M. & Tziperman, E. Coherent resonant millennial-scale climate oscillations triggered by massive meltwater pulses. *Journal of Climate* **16**, 2569–2585 (2003).

57. Desroches, M. *et al.* Mixed-mode oscillations with multiple time scales. *Siam Review* **54**, 211–288 (2012).

58. Theiler, J., Eubank, S., Longtin, A., Galdrikian, B. & Farmer, J. D. Testing for nonlinearity in time series: the method of surrogate data. *Physica D: Nonlinear Phenomena* **58**, 77–94 (1992).

Author contributions statement T.M. conceived the study and conducted the analyses with contributions from N.B. Both authors discussed and interpreted results. T.M. wrote the manuscript with contributions from N.B.

Acknowledgements The authors thank K. Riechers and M. Ben-Yami for their helpful comments. The authors acknowledge funding by the Volkswagen Foundation. This is TiPES contribution #X; The TiPES ("Tipping Points in the Earth System") project has received funding from the European Union's Horizon 2020 research and innovation programme under grant agreement No 820970. N.B. acknowledges further funding by the European Union's Horizon 2020 research and innovation programme under the Marie Sklodowska-Curie grant agreement No. 956170, as well as from the Federal Ministry of Education and Research under grant No. 01LS2001A.

Competing Interests The authors declare that they have no competing financial interests.

Correspondence Correspondence and requests for materials should be addressed to Takahito Mitsui (email: takahito321@gmail.com).

Supplementary Information (SI) Appendix https://github.com/takahito321/Predictability-of-DO-cooling/blob/main/EWS_DO_cooling_arXiv_SI.pdf

Figures

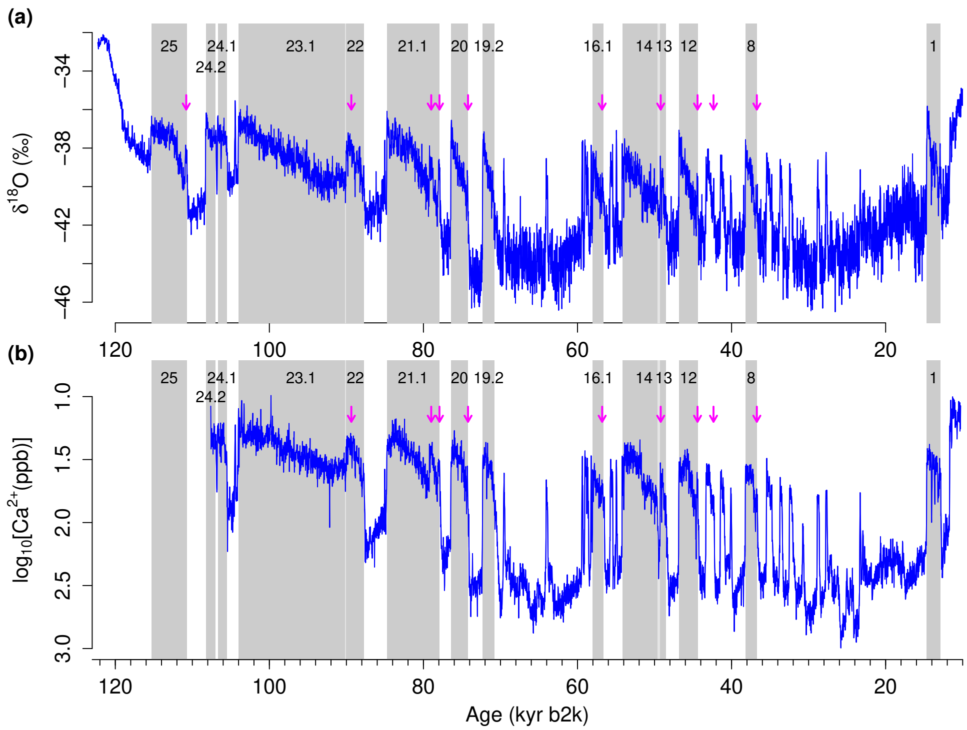

Figure 1. Greenland records from the NGRIP ice core: (a) δ^{18}O and (b) $\log_{10}[Ca^{2+}]$[20,21]. The interstadial parts longer than 1000-yr are highlighted with grey shades; their numbering is given at the top of each record[20]. The rebound events are indicated by arrows (see Methods for their list). Both records are presented at 20-yr resolution. The $\log_{10}[Ca^{2+}]$ record is available only up to DO-24.1. The compositions of GI-23.1 and GI-22, as well as of GI-14 and GI-13, are considered individual long interstadials[20,41]. The vertical axis for $\log_{10}[Ca^{2+}]$ in (b) is reversed to ease visual comparison with the δ^{18}O record.

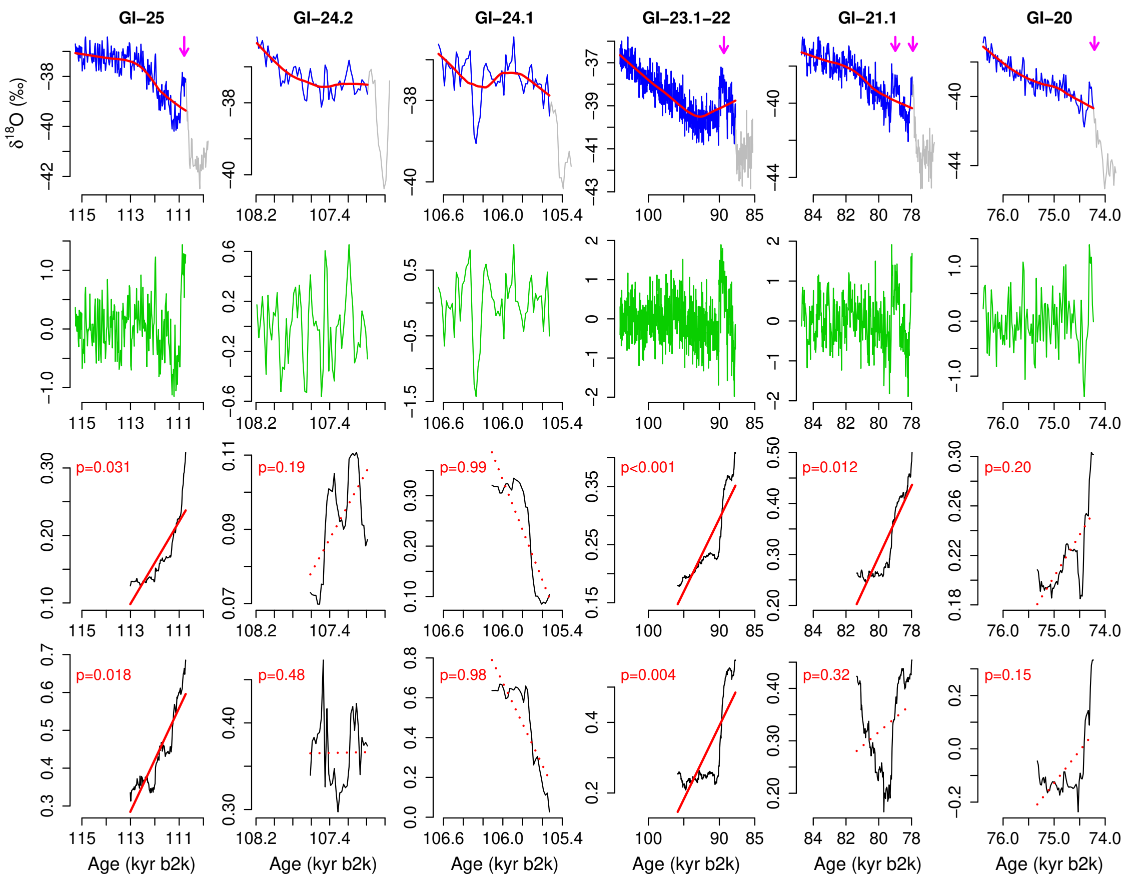

Figure 2. Analysis of CSD-based precursor signals of abrupt DO cooling transitions, for the first 6 interstadials of NGRIP δ^{18}O, from 115 ka to 74 kyr b2k. (Top row) Interstadials longer than 1000 yr (blue). The cooling transition and stadial parts are shown in grey[20]. Nonlinear trends are calculated with the Locally Weighted Scatterplot Smoothing (LOESS) (red). The smoothing span α that defines the fraction of data points involved in the local regression is set to 50% of each segment length. The rebound events are indicated by arrows (Methods). (Second row) Residuals (green) resulting from subtracting the nonlinear trends (red) from the records (blue). (Third row) Variance estimate in rolling windows (black) with size equal to 50% of each segment length. Values are plotted at the right edge of each rolling window. The linear trend is shown by a solid red line for

$p < 0.05$, by a dashed red line for $0.05 < p < 0.1$, and by a dotted line for $p > 0.1$. (Fourth row) Same as third row but for the lag-1 autocorrelation (i.e., a lag of 20 yr).

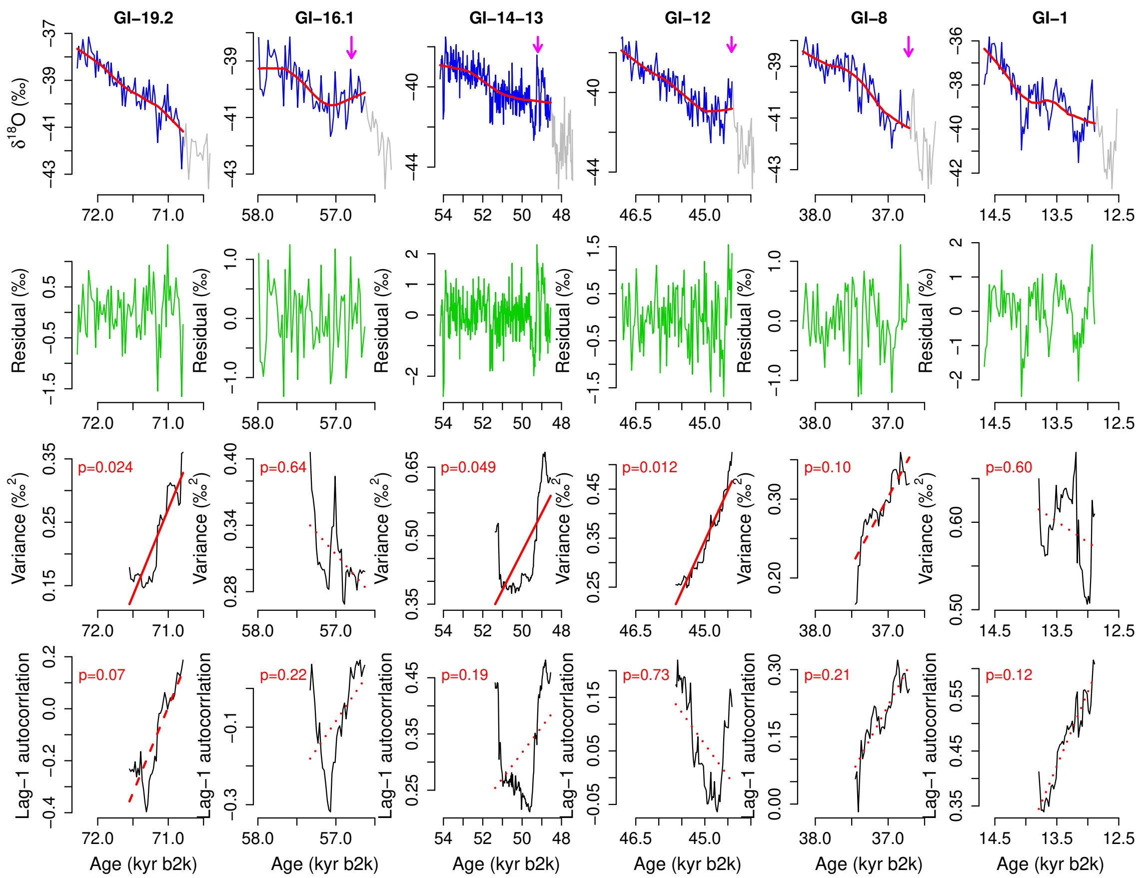

541 **Figure 3.** Same as Fig. 2 but for the following 6 interstadials, from 74 ka to 12 kyr b2k.

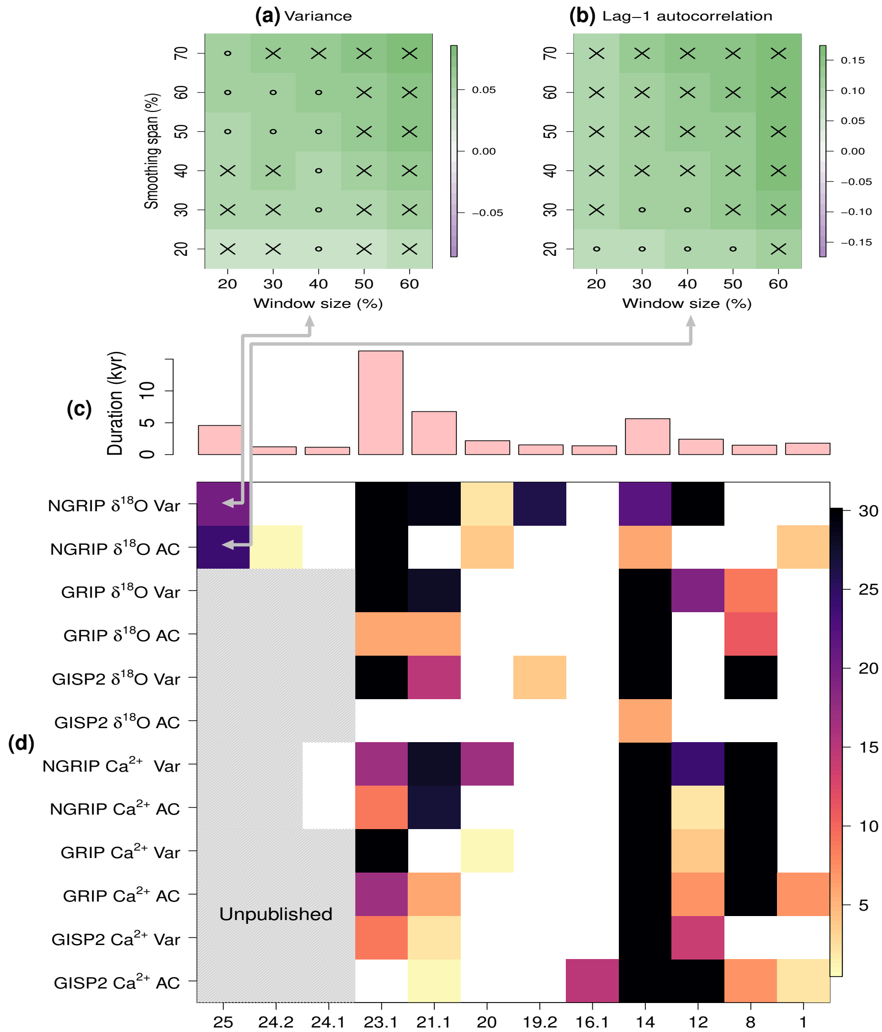

Figure 4. Detection of precursor signals of DO cooling transitions for different interglacials, different proxy variables, different ice cores, and different CSD indicators. (a,b) Robustness analysis of precursor signals with respect to the smoothing span and the rolling window size (% of interstadial length): the case of GI-25 interstadial from the NGRIP δ^{18}O record. The CSD indicator is the variance in (a) and the lag-1 autocorrelation in (b). Cross marks (x) indicates statistically significant positive trend of the respective CSD indicator ($p < 0.05$) based on a phase surrogate test (Methods), small open circles (o) indicate barely significant positive trends ($0.05 < p < 0.1$) and

cells are left blank if $p > 0.1$. (c) Durations of interstadials longer than 1000 yr. (d) Robustness of finding precursor signals for DO cooling transitions. The color indicates the number significant ($p < 0.05$) positive trends in each of the 30 sets of the smoothing spans and the rolling window sizes as in (a) and (b). For the cases of grey-shaded cells, the data is not publicly available.

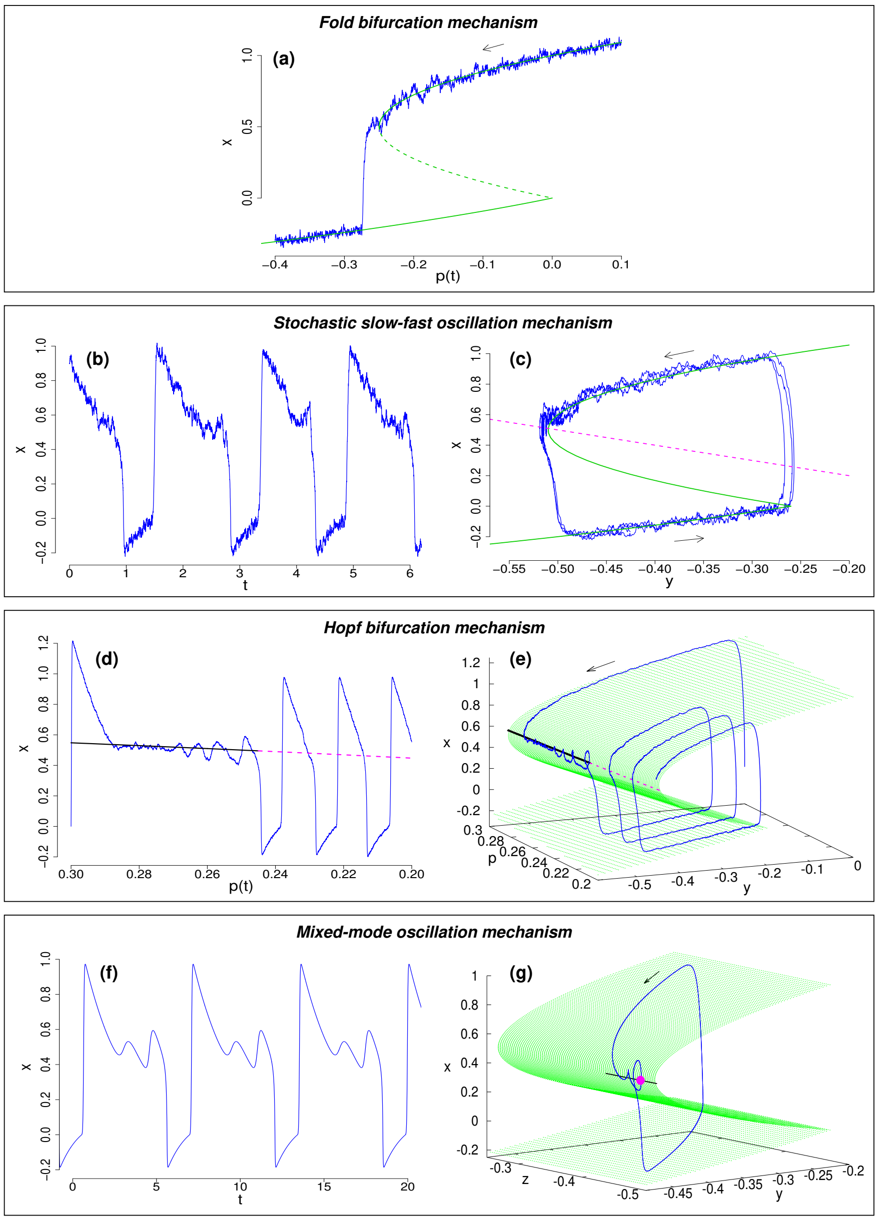
Fold bifurcation mechanism
(a)
x
p(t)
Stochastic slow-fast oscillation mechanism
(b)
(c)
x
t
y
Hopf bifurcation mechanism
(d)
(e)
x
p(t)
p
y
Mixed-mode oscillation mechanism
(f)
(g)
x
t
z
y

Figure 5. Four potential dynamical mechanisms for the DO cooling transitions (Methods): (a) Fold bifurcation mechanism. The time series $x(t)$ for decreasing $p(t)$ (blue). The green lines show the stable (solid) and unstable (dashed) fixed points. (b,c) Stochastic slow-fast oscillation mechanism of a FHN-type model. An example time series $x(t)$ is shown in (b) and the phase space trajectory (blue) in (c); the x-nullcline, i.e., the critical manifold, is shown in green. The y-nullcline is shown in dashed magenta. (d,e) Hopf bifurcation mechanism. An example time series $x(t)$ is shown in (d) as a function of $p(t)$. Stable (black, solid) and unstable (magenta, dashed) fixed points are also shown. The corresponding phase space trajectory $(x(t), y(t))$ for decreasing p is shown in (e) in blue. The critical manifold (green). (f,g) Mixed-mode oscillation mechanism. An example time series $x(t)$ is shown in (f) and the corresponding phase space trajectory in (g). The magenta dot is the saddle point with a stable manifold in the direction of the black segment; the trajectory is spiralling around it.